Journal of Solid State Chemistry 184 (2011) 1545–1550

Contents lists available at ScienceDirect

Journal of Solid State Chemistry

journal homepage: www.elsevier.com/locate/jssc

Synthesis and characterization of monodisperse, mesoporous, and magnetic sub-micron particles doped with a near-infrared fluorescent dye

Xavier Le Guével *, Robert Nooney, Colette McDonagh, Brian D. MacCraith

Biomedical Diagnostics Institute, School of Physical Sciences, Dublin City University, Glasnevin, Dublin 9, Ireland

ARTICLE INFO

Article history:
Received 27 January 2011
Received in revised form
5 April 2011
Accepted 9 April 2011
Available online 28 April 2011

Keywords:
Mesoporous material
NIR dye
Multifunctional particle
Magnetic core

ABSTRACT

Recently, multifunctional silica nanoparticles have been investigated extensively for their potential use in biomedical applications. We have prepared sub-micron monodisperse and stable multifunctional mesoporous silica particles with a high level of magnetization and fluorescence in the near infrared region using an one-pot synthesis technique. Commercial magnetite nanocrystals and a conjugated-NIR-dye were incorporated inside the particles during the silica condensation reaction. The particles were then coated with polyethyleneglycol to stop aggregation. X-ray diffraction, N_2 adsorption analysis, TEM, fluorescence and absorbance measurements were used to structurally characterize the particles. These mesoporous silica spheres have a large surface area (1978 m^2/g) with 3.40 nm pore diameter and a high fluorescence in the near infrared region at $\lambda = 700$ nm. To explore the potential of these particles for drug delivery applications, the pore accessibility to hydrophobic drugs was simulated by successfully trapping a hydrophobic ruthenium dye complex inside the particle with an estimated concentration of 3 wt%. Fluorescence imaging confirmed the presence of both NIR dye and the post-grafted ruthenium dye complex inside the particles. These particles moved at approximately 150 μm/s under the influence of a magnetic field, hence demonstrating the multifunctionality and potential for biomedical applications in targeting and imaging.

© 2011 Elsevier Inc. All rights reserved.

1. Introduction

Since the first synthesis of silica particles containing an ordered hexagonal array of mesopores in 1992 [1] there has been much interest in the applications of these materials in catalysis[2,3], separation science [4], sensors for metal ion recovery [5], and enzymes or DNA delivery [6–9]. Mesoporous silica particles have many unique properties, such as ordered porous structure, extremely high surface area ($> 1000\ m^2\ g^{-1}$), large pore volume, and a well-defined and tunable pore size (1.5–10 nm) [6,10–14]. Combining mesoporous silica with magnetic nanoparticles produces a hybrid particle that can be manipulated through the use of a magnetic field. A major advantage of the application of hybrid particles for biomedical purposes is that they can have multiple properties integrated within one single carrier particle, such as fluorescence, magnetism, cellular labelling, and/or therapeutic functions. These properties are integrated into mesoporous silicate particles through the addition of organic functionalities along the pore walls and exterior surfaces [15]. These materials can be moved quickly to specific target locations, in-vivo or in-vitro, and have a significant potential in drug delivery, medical diagnostics, and magnetic resonance imaging [10,14,16–18].

Some applications of multifunctional biomedical particles require fluorescence emission in the near-infrared (NIR). In this region, radiation can penetrate skin and overlying tissue as deep as a few millimetres, and such applications can be used in non-invasive medical diagnostics [19,20]. Furthermore, NIR fluorescence generally exhibits relatively low levels of background interference, since few naturally occurring molecules undergo electronic transitions in such a low-energy region. Even though there are many examples of mesoporous silica particles containing multiple fluorophores in the visible range [21–23], there are few examples of cost effective bright near infrared dye doped mesoporous magnetic silica particles.

In this work, we describe the one-pot synthesis of magnetic mesoporous silica particles with an average diameter of 500 nm. A near-infrared fluorophore is covalently bound inside the silica wall and particles are coated with polyethylene groups to improve colloidal stability. The pores are then loaded with a hydrophobic ruthenium dye complex to demonstrate post-synthesis grafting for applications such as drug delivery. Full characterization was done at each step to confirm the monodispersity, stability, mesostructured order, magnetism, and fluorescence properties of this material. The key features of the work include: (i) encapsulation in the silica nanoparticle of a bright, relatively

* Corresponding author. Fax: +353 1 700 8221.
E-mail address: xavier.leguevel@dcu.ie (X. Le Guével).

0022-4596/$ - see front matter © 2011 Elsevier Inc. All rights reserved.
doi:10.1016/j.jssc.2011.04.022

cheap, Cy5-like NIR fluorescent label; (ii) co-encapsulation of magnetic nanocrystals to enable nanoparticle movement and control; and (iii) post-grafting of a hydrophobic fluorescent ruthenium complex into the mesopores as a surrogate drug to simulate drug delivery and to enhance the multifunctionality of the particle.

2. Experimental

2.1. Materials

Polyvinyl pyrrolidone (PVP10, average MW 10 000 g/mol), cetyltrimethylammonium 99% (CTAB), tetraethyl orthosilicate 99.99% (TEOS), 3-mercaptopropyltriethoxysilane (MPTES), dimethylsulphoxide 99.9% (DMSO), anhydrous *n*-hexanol, absolute ethanol, hydrochloric acid 37 wt%, hydroxide ammonium 28 wt%, 4,5-Benzo-5′-(iodoacetaminomethyl)-1′,3,3,3′,3′-pentamethyl-1-(4-sulfobutyl)indodicarbocyanine 90% (NIR-664-Iodoacetamide) and Tris (4,7-diphenyl-1,10-phenanthroline)ruthenium(II) dichloride complex ($Ru(dpp)_3Cl_2$) were purchased from Sigma-Aldrich. 2-Methoxy(polyethyleneoxy)propyl trimetoxysilane 90% (PEG-silane) was purchased from ABCR Chemicals and 3-mercaptoethoxysilane was obtained from FluoroChem. Superparagmagnetic iron oxide nanocrystals (SPIO, $\varnothing = 8$ nm, 45–60 emu/g, 19 mg/mL in chloroform, eq.$\sim$21.6 nmol/mL) coated with oleic acid and oleylamine were purchased from Ocean NanoTech, LLC. Deionized water $> 18\ M\Omega$ was used from a Millipore academic system. All chemicals were used without further purification.

2.2. Preparation of mesoporous magnetic fluorescent silica particles

Hydrophobic SPIO nanocrystals (10 mg), dispersed in chloroform, were mixed with an aqueous solution of CTAB (0.1 M, 10 mL H_2O) containing PVP10 (0.1 g). The water/oil emulsion was ultrasonicated for 3 h to achieve: (I) phase transfer of the SPIO nanocrystals to the aqueous phase, and (II) evaporation of the chloroform. The resultant translucent black solution was filtered (0.2 μm; polypropylene syringe) to remove any remaining aggregates.

The conjugation of NIR-664-Iodoacetamide dye (3 mg) to MPTES (2 molar excess) was performed in anhydrous *n*-hexanol (3.5 mL), under a nitrogen atmosphere, in the dark, with 4 h of stirring. Separately, aqueous SPIO nanocrystal solution (1 mL) was added to a water/ethanol solution (6 mL, volume ratio 1/1) and heated to 50 °C. The pH was adjusted to between 9 and 10 with the addition of ammonium hydroxide (116 μL, 28 wt% in H_2O). Following this TEOS (50 μL) and conjugated dye/MPTES (10 μL) were added under vigorous stirring. After 1 h, PEG-silane (30 μL) was added and the solution stirred for 24 h at 50 °C. The resultant mesoporous silica particles were centrifuged at 10,000 rpm for 10 min. The particles were resuspended in acidic ethanol (30, 70 μL of HCL 37 wt%) and heated at 50 °C for 5 h to remove CTAB from the mesopores. The mixture was then washed 2 times in water and filtered by magnetic separation using a permanent magnet (Block 10x5 × 1 mm, Supermagnete®, Gottmadingen-Germany) to produce a brown orange solution. The NIR dye-doped magnetic mesoporous particles in solution are referred to as **MMP** in the remaining part of the document.

2.3. Post-grafting of a ruthenium dye complex

$Ru(dpp)_3Cl_2$ powder (2 mg; 1.7 μmol) was dissolved in DMSO (2 mL). Aqueous MMP solution (2 mL, 1 mg/mL) was centrifuged, and added to the fluorescent DMSO solution and stirred at room temperature for 3 h. The bright orange product was washed 3 times in water and filtered again using a permanent magnet to remove all the free dye in solution. The ruthenium doped MMP (**Ru-MMP)** were stable in aqueous solution due to the continued presence of PEG groups on the surface.

2.4. Characterization

UV-visible extinction spectra of colloidal suspensions of the particles were measured using a Cary 50 scan UV-visible spectrophotometer (Varian) in transmission mode. Fluorescence measurements were performed on a Safire (Tecan) microplate reader. TEM micrographs were obtained using a Hitachi 7000 transmission electron microscope operated at 100 kV. Samples were prepared by dropping aqueous solutions of the particles onto a formvar carbon-coated copper grid. Images were captured digitally using a Megaview 2 CCD camera. The dynamic light scattering (DLS) and the zeta potential measurements were performed on a Delsa Nano C instrument from Beckman Coulter. Powder X-ray diffraction (XRD) was run on a Bruker-AXS D8 (Siemens) X-ray diffractometer using filtered Cu $K\alpha$ radiation ($\lambda = 0.154$ nm) at 45 kV and 20 mA. Data were collected by step scan with a step size of 0.01° and a step time of 1.0 s. Particles were characterized by nitrogen sorption measurements, performed on a Quantochrome Instrument Nova 4000e at 77 K. Prior to measurements, samples were degassed at 25 °C for 24 h. The surface area was calculated using the BET (Brunauer, Emmett and Teller) and the pore size using the BJH (Barrett, Joyner and Halenda) method. Fluorescence microscopy images were obtained using an Olympus IX71 inverted epifluorescence microscope equipped with a Nikon D1X digital CCD camera. We used a UPlan Fluorite phase-contrast objective (magnification, 10; numerical aperture, 0.3) for fluorescence observations. Particles were visualized using two different filters: (i) a wide-band-pass excitation filter (460–490 nm), emission filter (515–550 nm) and a dichromatic mirror at 505 nm (U-MWIB; Olympus) and (ii) a wide-band-pass excitation filter (590–650 nm) and emission filter (663–737 nm). The movement of the particles in the presence of a permanent magnet was also recorded with both filters.

3. Result and discussion

3.1. Synthesis procedure

In this work the synthesis of MMP was divided into two key stages: firstly, the transfer of the SPIO nanocrystals from the organic phase to an aqueous media, and secondly, self assembly of the mesoporous particles. For SPIO nanocrystal transfer, the hydrophobic oleic acid was substituted with CTAB stabilising agent. PVP was also added as a co-surfactant to improve the transfer efficiency and reduce the number of aggregates in the solution [24]. CTAB present in the aqueous SPIO nanocrystals solution also acted as an organic template in the formation of the mesoporous silica spheres. Standard base catalysis conditions were used for self assembly, in an ethanol/water mixture, at a temperature between 40 and 70 °C for [12,15]. Using only water as a solvent led to the formation of non-spherical and polydispersed mesoporous particles while using mainly ethanol as a solvent led to the formation of smooth and spherical particles but without the presence of mesopores. Thus, a compromise was found to obtain monodispersed spherical particles with a relative mesostructured order. The extraction of the surfactant CTAB from the pores was done in the acidic condition, in preference to calcination, because calcination destroyed the organic dye inside the silica walls and also led to aggregation of the particles.

3.2. Structure and morphology of MMP particles

Fig. 1a–c shows TEM pictures of the MMP at different magnifications. The particles are 515 ± 30 nm in diameter and monodispersed with a smooth spherical surface. The diameter measured from the dynamic light scattering (Fig. 1d), agrees well with TEM. The absence of larger aggregates in the DLS spectra indicates that the nanoparticles form a stable colloidal suspension. This stability is due to the addition of polyethyleneglycol. The particles have a significantly negative zeta potential ($\zeta = -35.10$ mV) which indicates that the particles are stabilised by electrostatic repulsion. Without the addition of PEG-silane the particles precipitated in less than 2 min. This aggregation is caused by the interparticle hydrogen-bonding and van der Waals interaction between the surface silanol groups.

At high magnification (Fig. 1c) we can see the porous structure of the silica network. From XRD analysis at low-angle, shown in Fig. 2a, a peak at $2\theta = 2.5^\circ$ was obtained and assigned to the reflection peak (1 0 0) of a hexagonal mesoporous structure. Using Bragg's law, the d_{100} spacing is approximately 3 nm. The physical properties of MMP were analyzed by nitrogen sorption–desorption isotherms (full data shown in supplementary information Figure S1). The pore size diameter (3.40 nm), the total pore volume (2.858 cm^3/g) and surface area (1978 m^2/g) were obtained using the Barrer–Joyner–Halenda (BJH) and the BET models (Fig. 2b). The pore size distribution determined by BJH is in agreement with the data obtained by XRD in the order of 3–4 nm diameter. Furthermore, the high specific area over 1000 m^2/g of this material is typical of a mesoporous structure.

The crystalline structure of the commercial magnetite Fe_3O_4 in the MMP was confirmed by XRD (Fig. 2c and S2 for a full range $2\theta = 20$–68°), where the presence of a characteristic peak at $2\theta = 35^\circ$ was indexed to Fe_3O_4 using the International Centre of Diffraction file for magnetite. From the TEM micrographs we can clearly see the presence of magnetite inside the MMP, which have a higher contrast to the lower density silica matrix. No iron oxide nanoparticles were observed outside the silica spheres. This indicates that a high percentage of the magnetite was incorporated in the MMP during the self-assembly process. Upon placing a permanent magnet close to an aqueous suspension of MMP (1 mg/mL), all the particles moved quickly to the magnet in less a minute indicating high magnetization (Fig. 2d).

3.3. Spectroscopic properties of dyes

Mesoporous silica spheres can be used to carry and deliver hydrophobic drugs into human cancer cells [25,26]. It has been established that hydrophobicity enhances cytotoxicity, hence many drugs are hydrophobic in nature [27–29]. In this work, we wish to prove the concept of drug delivery, hence enhance the

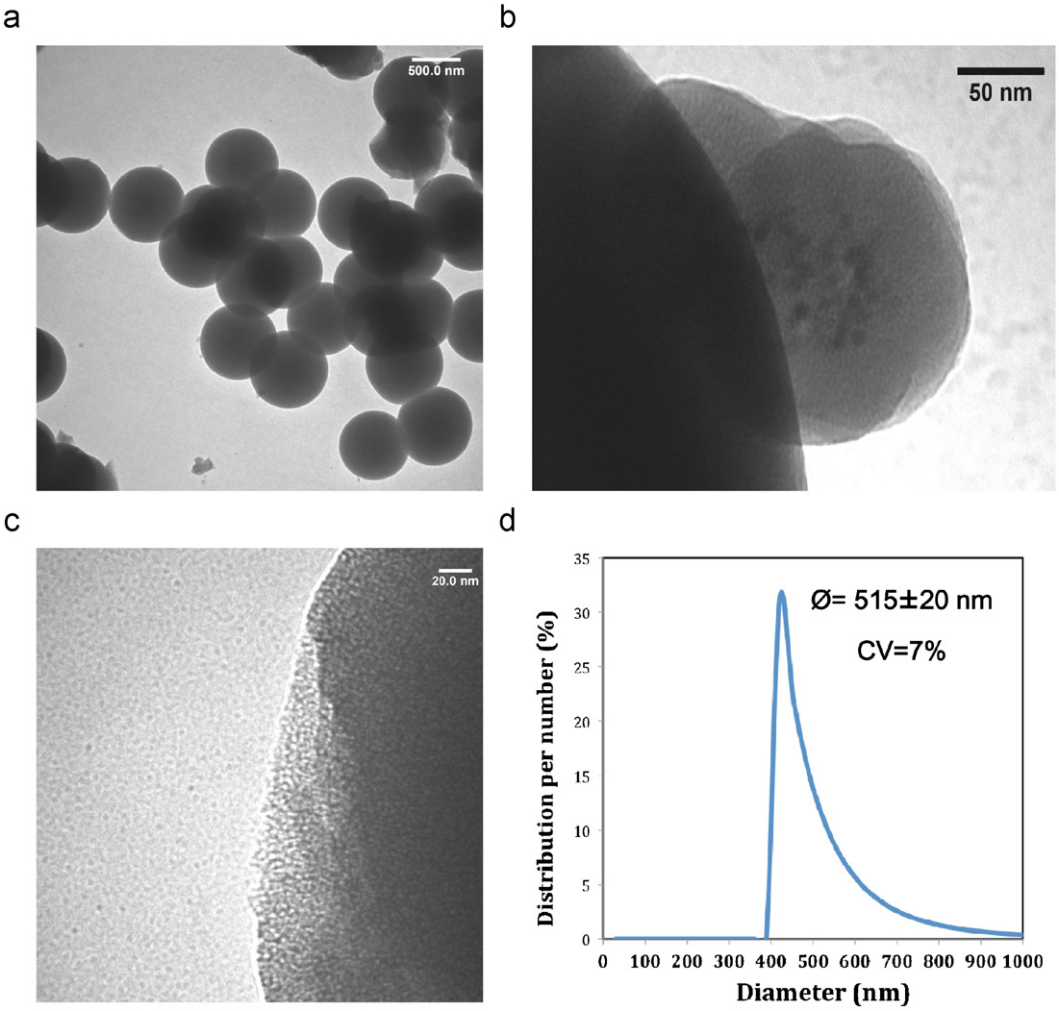

Fig. 1. Transmission electron micrographs (a–c) and dynamic light scattering (d) measurements of **MMP** solution. Several magnetic NPs, approximately 515 nm in diameter, can be seen in the particle in (b) and mesoporous structures are clearly visible in (c). The DLS results in (d) indicate a monodisperse distribution of nanoparticles in agreement with micrograph with a standard deviation (CV) lower than 10%.

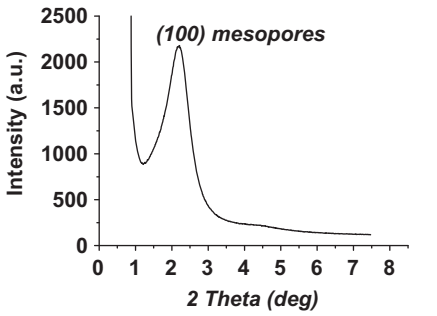

b

Samples	S_{BET} (m^2/g)[a]	D_{BJH} (nm)[b]	Vt (cm^3/g)[c]	$DXRD$ (nm)[d]
MMP	1978	3.40	2.858	3- 4
Ru-MMP	764	3.40	1.154	3- 4

[a]S_{BET} : BET surface area calculated from data at P/P_0 = 0.01-0.3. [b]D_{BJH} : pore diameter assigned from the maximum on the pore size distribution. [c]Vt : total pore volume calculated at P/P_0 at 0.99. [d]D_{XRD} : pore size is determined using the Bragg Law $n\lambda = 2d\sin\theta$ with $2\theta = 2.5^o$, λ= 0.154 nm and n = 1.

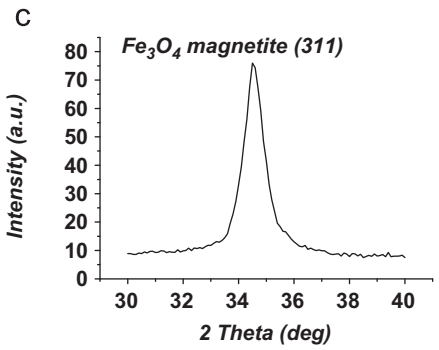

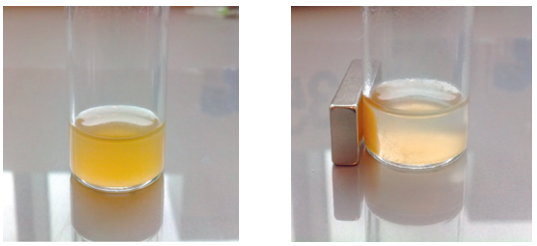

Fig. 2. Low-angle (a) and wide-angle (c) XRD patterns of **MMP** powder confirm the mesoporous property of the silica nanoparticles and the presence of the magnetic core; (b) nitrogen sorption analysis (BET/BJH) of **MMP** and **Ru-MMP** powders indicate the high surface specific area and the reduction of the porosity after post-grafting with the ruthenium complex; (d) photographs showing magnetic capture of **MMP** suspension.

multifunctionality of the particles by inserting a hydrophobic fluorescent dye in the pores of the MMP particles. For this purpose, we used a ruthenium organometallic complex, the fluorescence of which was used to monitor the encapsulation process and to estimate the efficiency of encapsulation. This dye is already being tested in clinical trials as a complexing agents against cancer tumours and is therefore a good choice for the purpose of this investigation [30]. The excitation/emission fluorescence wavelength of the ruthenium dye is at 455/615 nm with a quantum efficiency of 36.6% and a molar absorptivity of 28,600 $Lmol^{-1}\,cm^{-1}$ [31].

As well as the ruthenium complex (surrogate drug), we also covalently doped the particles with a red dye which would enable the particles to be used as fluorescent labels to monitor the drug delivery process and for imaging. The NIR664 dye, from Few Chemicals, has a quantum efficiency of 23%, and a molar absorptivity of 187,000 $Lmol^{-1}\,cm^{-1}$, with excitation and emission wavelengths of 672 and 694 nm, respectively, in isopropanol. This dye was chosen because it is relatively inexpensive compared to other cyanine dyes, e.g., CyDye™ or Alexa Flour dyes, but with a similar optical properties.

3.4. Optical response of MMP and Ru-MMP

The MMP sample containing the NIR dye only exhibits a high fluorescence signal in the near-infrared region with a maximum intensity at λ=700 nm proving the stability of the near infrared dye NIR664 in the silica spheres (Fig. 3a). These particles did not leach any dye over two months of analysis thus confirming that the dye has been covalently entrapped inside the particle. After post-grafting, the Ru-MMP particle exhibits the strong broad absorption band of the ruthenium complex located at λ=450 nm (Fig. 3b) and the fluorescence emission peak at λ=634 nm indicating the presence of ruthenium dye in the mesoporous material. Ru-MMP also presents the same NIR fluorescence as MMP (not shown) indicating no modification of the NIR dye inside the particles. Fig. 3c shows the absorption in the region of 600 nm of MMP before and after post-grafting. The relative fluorescence intensity values have been determined on the microplate reader for MMP and Ru-MMP samples in the optimum conditions (wavelengths and gain) for the NIR664 dye and for the ruthenium dye. The data, collected in Fig. 3d, show no modification of the relative fluorescence intensities of the NIR dye for both samples. After post-grafting, we observed a 2000-fold increase of the relative fluorescence intensity at $\lambda \sim 600$ nm due to the presence of the ruthenium complex. The relative loading of the ruthenium dye into the mesoporous silica sphere was estimated from the significant decrease of the BET specific area from 1978 to 764 m^2/g and a reduction in the total pore volume from 2.858 to 1.154 cm^3/g (Fig. 2b) after post-grafting. The reduction of the pore volume by dye loading corresponds roughly to 40%. From absorption measurements we estimate that the particles contain 3% (w/w) ruthenium dye. TEM images of Ru-MMP (Figure S3) showed a rough surface in comparison with MMP and indicate that the $Ru(dpp)_3Cl_2$ is also grafted onto the surface of the particles. Therefore the reduction in pore volume is most likely due to pore blocking of the $Ru(dpp)_3Cl_2$ on the surface of the particle.

Aqueous suspensions of both MMP and Ru-MMP (1 mg/mL) were investigated using fluorescence microscopy to determine both the fluorescence intensity and influence of a magnetic field on the properties of the particles. We used two different filters sets, as described in Section 2, to match the ruthenium dye and the NIR dye, respectively. From the images, the NIR fluorescence of MMP and Ru-MMP is clearly visible, respectively, in Fig. 4a and b. The slight reduction of intensity for the ruthenium-doped particles is due to a change in the concentration of particles on the plastic chamber. Fig. 4c and d shows fluorescence images of MMP and Ru-MMP using the filter matching the emission of the

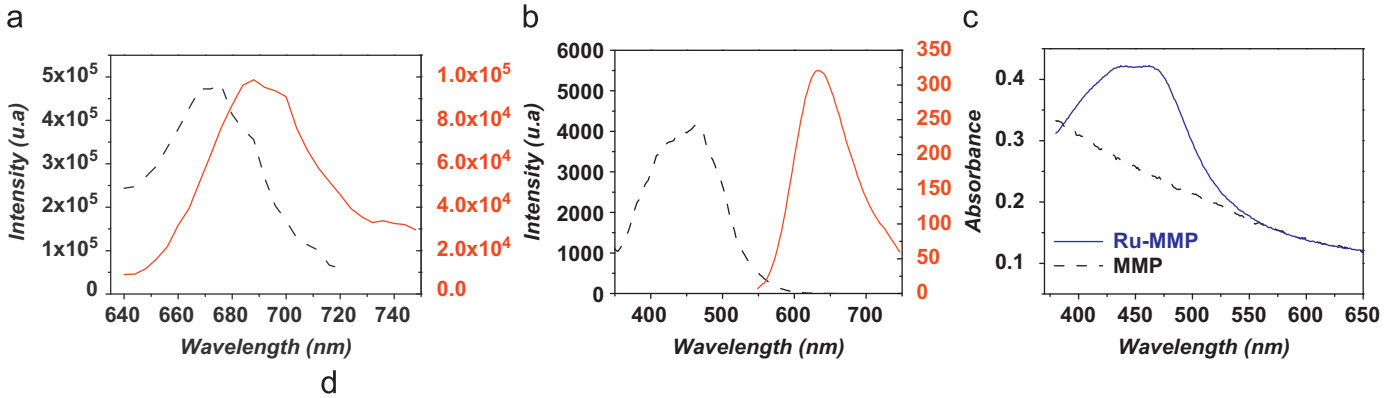

d

	Relative fluorescence intensity at $\lambda_{em.}$= 700 nm *	Relative fluorescence intensity at $\lambda_{em.}$= 600 nm **
MMP	404.1	1.3
Ru-MMP	365.2	2024.0

Fig. 3. (a) Excitation (dashed line)/emission (solid line) spectra of the MMP particles showing the presence of the NIR dye and (b) corresponding absorption and emission spectra for Ru-MMP particles in the lower wavelength range indicating the presence of the ruthenium complex. (c) Absorption spectrum of MMP before (dashed line) and after ruthenium uptake. Relative fluorescence measurements gathered in the Table (d) were determined in a microplate reader for **MMP and Ru-MMP** at the maximum emission of the NIR664 and $Ru(dpp)_3$ dyes at different gain. Results indicate the presence of the ruthenium dye in the particle for Ru-MMP and the absence of quenching of the NIR dye. * λ_{exc}=670 nm; Gain=81 ** λ_{exc}=450 nm; Gain=69.

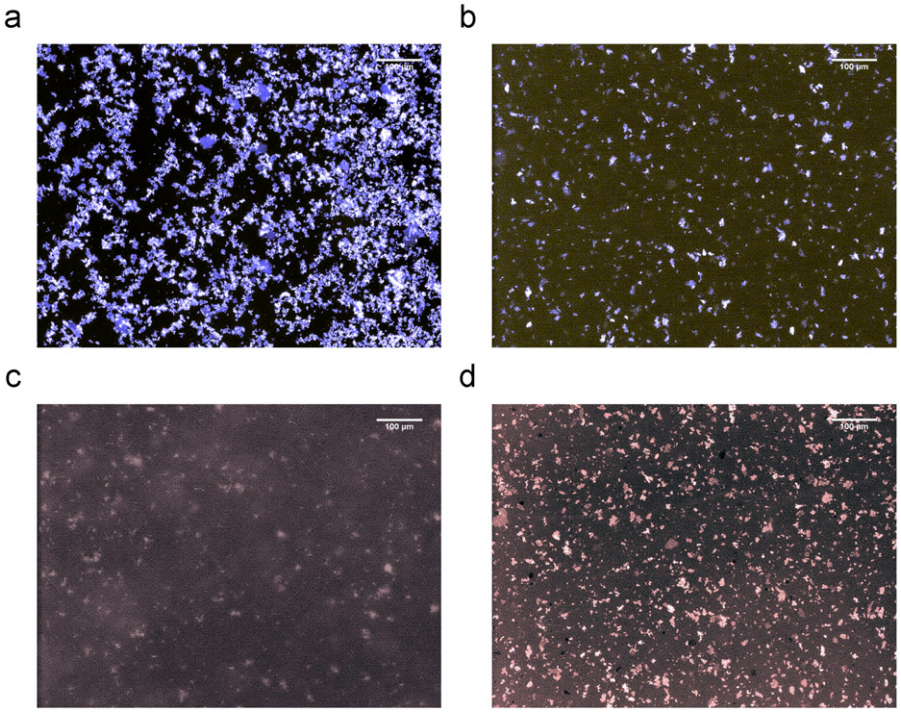

Fig. 4. Fluorescence microscopy measurements of **MMP** and **Ru-MMP** in the near infrared region (663–737 nm) (in blue colour, respectively (a) and (b) for MMP and Ru-MMP) and in the orange region (515–550 nm) (in orange colour, respectively, (c) and (d) for MMP and Ru-MMP). Bars, 100 μm. (For interpretation of the references to color in this figure legend, the reader is referred to the web version of this article.)

ruthenium complex. The mesoporous particles doped with ruthenium exhibit a strong intensity and particles are clearly visible. The weak intensity under an excitation wavelength 460–490 nm for the MMP, without ruthenium dye, is due to the near-infrared dye which has a second low fluorescence excitation/emission profile at short wavelengths (Figure S4). Hence, the fluorescence microscopy data validate the results on the microplate experiments for fluorescence detection of the ruthenium dye after incorporation in the particles. Furthermore, the mesoporous silica particles after post-grafting maintain almost the same fluorescence value as the MMP sample in the near-infrared region indicating no relevant degradation and quenching of the near infrared dye.

To show the magnetic property of these particles and visualize them, a permanent magnet was placed on the top of the chamber containing MMP particles. Particle diffusion was recorded for 50 s (movie available in supplementary material) using a filter matching the fluorescence emission in the near-infrared region. As is expected, the particles show a rapid diffusion and concentration with an average velocity of approximately 150 μm/s thus confirming the ability of these multifunctional particles to be

detected in the NIR region and to be moved for example in a microfluidic device.

4. Conclusion

Multifunctional and mesostructured magnetic silica particles were synthesized with a near infrared dye covalently attached to the silica matrix. The 500 nm particles are highly monodisperse and stable in an aqueous solution with a polyethyleneglycol coating. The particles exhibit an intense fluorescence in the near-infrared region at $\lambda = 700$ nm under $\lambda \sim 670$ nm excitation light. The investigation of the mesostructure and the pore size by X-ray diffraction and nitrogen sorption show the presence of 3–4 nm pores and a large surface area of 1978 m^2/g. The incorporation of magnetite (Fe_3O_4) nanocrystals provide high magnetization for bead separation. To show the potential of mesoporous magnetic fluorescent particles for drug delivery application, a hydrophobic dye which simulates the drug, was successfully entrapped in the mesopores. Structural, optical and microscopy characterization validates the post-grafting of the dye inside the mesoporous material. These results show the great potential of magnetic mesoporous silica particles for simultaneous imaging in the near infrared region and targeted drug delivery.

Aknowledgement

This material is based upon work supported by the Science Foundation Ireland under Grant no 05/CE3/B754.

Appendix A. Supplementary material

Supplementary data associated with this article can be found in the online version at doi:10.1016/j.jssc.2011.04.022.

References

[1] C.T. Kresge, M.E. Leonowicz, W.J. Roth, J.C. Vartuli, J.S. Beck, Nature 359 (6397) (1992) 710–712.
[2] R.J.P. Corriu, E. Lancelle-Beltran, A. Mehdi, C. Reye, S. Brandes, R. Guilard, Journal of Materials Chemistry 12 (5) (2002) 1355–1362.
[3] Y. Kim, P. Kim, C. Kim, J. Yi, Journal of Materials Chemistry 13 (9) (2003) 2353–2358.
[4] H.S. Zhou, H. Sasabe, I. Honma, Journal of Materials Chemistry 8 (3) (1998) 515–516.
[5] K.Z. Hossain, L. Mercier, Advanced Materials 14 (15) 1053 14 (15) (2002).
[6] M. Fujiwara, F. Yamamoto, K. Okamoto, K. Shiokawa, R. Nomura, Analytical Chemistry 77 (24) (2005) 8138–8145.
[7] Y. Li, B. Yan, C.H. Deng, W.J. Yu, X.Q. Xu, P.Y. Yang, X.M. Zhang, Proteomics 7 (14) (2007) 2330–2339.
[8] I.I. Slowing, B.G. Trewyn, V.S.Y. Lin, Journal of the American Chemical Society 129 (28) (2007) 8845–8849.
[9] F. Torney, B.G. Trewyn, V.S.Y. Lin, K. Wang, Nature Nanotechnology 2 (5) (2007) 295–300.
[10] Y.J. Han, G.D. Stucky, A. Butler, Journal of the American Chemical Society 121 (42) (1999) 9897–9898.
[11] S.S. Huang, Y. Fan, Z.Y. Cheng, D.Y. Kong, P.P. Yang, Z.W. Quan, C.M. Zhang, J. Lin, Journal of Physical Chemistry C 113 (5) (2009) 1775–1784.
[12] M. Liong, S. Angelos, E. Choi, K. Patel, J.F. Stoddart, J.I. Zink, Journal of Materials Chemistry 19 (35) (2009) 6251–6257.
[13] T.R. Sathe, A. Agrawal, S.M. Nie, Analytical Chemistry 78 (16) (2006) 5627–5632.
[14] M. Vallet-Regi, F. Balas, D. Arcos, Angewandte Chemie-International Edition 46 (40) (2007) 7548–7558.
[15] V. Cauda, A. Schlossbauer, J. Kecht, A. Zurner, T. Bein, Journal of the American Chemical Society 131 (32) (2009) 11361–11370.
[16] N. Kohler, C. Sun, A. Fichtenholtz, J. Gunn, C. Fang, M.Q. Zhang, Small 2 (6) (2006) 785–792.
[17] M. Liong, J. Lu, M. Kovochich, T. Xia, S.G. Ruehm, A.E. Nel, F. Tamanoi, J.I. Zink, ACS Nano 2 (5) (2008) 889–896.
[18] Z. Medarova, W. Pham, C. Farrar, V. Petkova, A. Moore, Nature Medicine 13 (3) (2007) 372–377.
[19] A.A. Burns, J. Vider, H. Ow, E. Herz, O. Penate-Medina, M. Baumgart, S.M. Larson, U. Wiesner, M. Bradbury, Nano Letters 9 (1) (2009) 442–448.
[20] X. Le Guevel, B. Hötzer, G. Jung, M. Schneider, Journal of Materials Chemistry 10 (2011) 1039/c0jm02660c.
[21] S. Ernst, M. Selle, Microporous and Mesoporous Materials 27 (2-3) (1999) 355–363.
[22] F. Marlow, M.D. McGehee, D.Y. Zhao, B.F. Chmelka, G.D. Stucky, Advanced Materials 11 (8) 632-+.
[23] Y.F. Yao, M.S. Zhang, J.X. Shi, M.L. Gong, H.J. Zhang, Y.S. Yang, Materials Letters 48 (1) (2001) 44–48.
[24] Y.S. Lin, C.L. Haynes, Chemistry of Materials 21 (17) (2009) 3979–3986.
[25] Z.M. Tao, B.B. Toms, J. Goodisman, T. Asefa, Chemical Research in Toxicology 22 (11) (2009) 1869–1880.
[26] J.L. Vivero-Escoto, I.I. Slowing, C.W. Wu, V.S.Y. Lin, Journal of the American Chemical Society 131 (10) (2009) 3462–3463.
[27] Y.Q. Tang, S.Y. Liu, S.P. Armes, N.C. Billingham, Biomacromolecules 4 (6) (2003) 1636–1645.
[28] H.G. Zhu, M.J. McShane, Journal of the American Chemical Society 127 (39) (2005) 13448–13449.
[29] K.M. Wasan, D.R. Brocks, S.D. Lee, K. Sachs-Barrable, S.J. Thornton, Nature Reviews Drug Discovery 7 (1) (2008) 84–99.
[30] A. Levina, A. Mitra, P.A. Lay, Metallomics 1 (6) (2009) 458–470.
[31] K.J. Morris, M.S. Roach, W.Y. Xu, J.N. Demas, B.A. DeGraff, Analytical Chemistry 79 (24) (2007) 9310–9314.